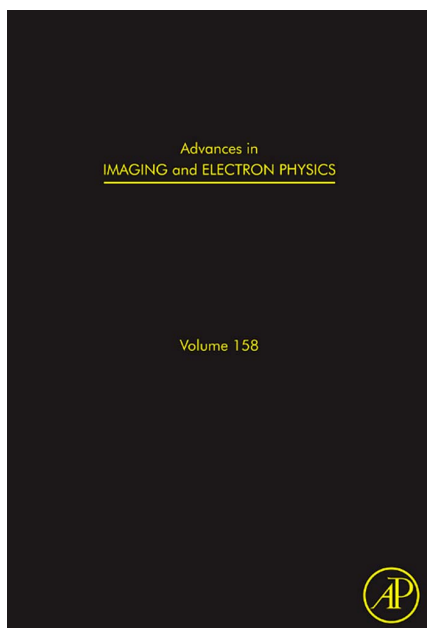


**Provided for non-commercial research and educational use only.
Not for reproduction, distribution or commercial use.**

This chapter was originally published in the book *Advances in Imaging and Electron Physics*. The copy attached is provided by Elsevier for the author's benefit and for the benefit of the author's institution, for non-commercial research, and educational use. This includes without limitation use in instruction at your institution, distribution to specific colleagues, and providing a copy to your institution's administrator.



All other uses, reproduction and distribution, including without limitation commercial reprints, selling or licensing copies or access, or posting on open internet sites, your personal or institution's website or repository, are prohibited.

For exceptions, permission may be sought for such use through Elsevier's permissions site at:

<http://www.elsevier.com/locate/permissionusematerial>

From P. Dombi, Surface Plasmon-Enhanced Photoemission and Electron Acceleration with Ultrashort Laser Pulses. In: Peter W. Hawkes, editor: *Advances in Imaging and Electron Physics*, Vol 158, United States of America: Academic Press; 2009, pp. 1–26.

ISBN: 978-0-12-374769-3

© Copyright 2009 Elsevier Inc.
Academic Press

Chapter 1

Surface Plasmon-Enhanced Photoemission and Electron Acceleration with Ultrashort Laser Pulses

Péter Dombi

Contents		
	1. Introduction	2
	2. Electron Emission and Photoacceleration in Surface Plasmon Fields	3
	2.1. Emission Mechanisms	3
	2.2. Emission Currents	5
	2.3. Electron Acceleration in Evanescent Surface Plasmon Fields	7
	3. Numerical Methods to Model Surface Plasmon-Enhanced Electron Acceleration	7
	3.1. Elements of the Model	7
	3.2. Model Results	11
	4. Experimental Results	16
	4.1. Surface Plasmon-Enhanced Photoemission	16
	4.2. Generation of High-Energy Electrons	18
	4.3. Time-Resolved Studies of the Emission	19
	5. The Role of the Carrier-Envelope Phase	21
	5.1. Light-Matter Interaction with Few-Cycle Laser Pulses, Carrier-Envelope Phase Dependence	21
	5.2. Carrier-Envelope Phase-Controlled Electron Acceleration	22
	6. Conclusions	23
	Acknowledgments	24
	References	24

Research Institute for Solid-State Physics and Optics, Budapest, Konkoly-Thege M. út, Hungary

Advances in Imaging and Electron Physics, Volume 158, ISSN 1076-5670, DOI: 10.1016/S1076-5670(09)00006-8.
Copyright © 2009 Elsevier Inc. All rights reserved.

1. INTRODUCTION

It was shown recently that ultrashort, intense laser pulses are particularly well suited for the generation of electron and other charged particle beams both in the relativistic and the nonrelativistic intensity regimes of laser-solid interactions (Irvine, Dechant, & Elezzabi, 2004; Leemans et al., 2006, and references therein). One method to generate well-behaved, optically accelerated electron beams with relatively low-intensity light pulses is surface plasmon polariton (SPP)-enhanced electron acceleration. Due to the intrinsic phenomenon of the enhancement of the SPP field (with respect to the field of the SPP-generating laser pulse), substantial field strength can be created in the vicinity of metal surfaces with simple, high-repetition-rate, unamplified laser sources. This results in both SPP-enhanced electron photoemission and electron acceleration in the SPP field. SPP-enhanced photoemission was demonstrated in several experimental publications. Typical photocurrent enhancement values ranged from $\times 50$ to $\times 3500$ achieved solely by SPP excitation (Tsang, Srinivasan-Rao, & Fischer, 1991).

In addition to SPP-enhanced photoemission, the electrons in the vicinity of the metal surface can undergo significant cycle-by-cycle acceleration in the evanescent plasmonic field. This phenomenon, termed *SPP-enhanced electron acceleration*, was discovered recently and was experimentally demonstrated to be suitable for the production of relatively high-energy, quasi-monoenergetic electron beams with the usage of simple femtosecond lasers (Irvine et al., 2004; Kupersztych, Monchicourt, & Raynaud, 2001; Zawadzka, Jaroszynski, Carey, & Wynne, 2001). In this scheme, the evanescent electric field of SPPs accelerates photo-emitted electrons away from the surface. This process can be so efficient that multi-keV kinetic energy levels can be reached without external direct current (DC) fields (Irvine and Elezzabi, 2005; Irvine et al., 2004). This method seems particularly advantageous for the generation of well-behaved femtosecond electron beams that can later be used for infrared pump/electron probe methods, such as ultrafast electron diffraction or microscopy (Lobastov, Srinivasan, & Zewail, 2005; Siwick, Dwyer, Jordan, & Miller, 2003). These time-resolved methods using electron beams can gain importance in the future by enabling both high spatial and high temporal resolution material characterization at the same time. They will become particularly interesting if the attosecond temporal resolution domain becomes within reach with electron diffraction and microscopy methods, as suggested recently (Fill, Veisz, Apolonski, & Krausz, 2006; Stockman, Kling, Krausz, & Kleineberg, 2007; Varró and Farkas, 2008). Moreover, studying the spectral properties of femtosecond electron beams has the potential to reveal ultrafast excitation dynamics in solids and to provide the basis for a single-shot measurement tool of the carrier-envelope (CE) phase (or the optical waveform) of ultrashort laser

pulses, as we suggested recently (Dombi and Rácz, 2008a; Irvine, Dombi, Farkas, & Elezzabi, 2006). Other waveform-sensitive laser-solid interactions that have already been demonstrated (Apolonski et al., 2004; Dombi et al., 2004; Fortier et al., 2004; Mücke et al., 2004) suffer from low experimental contrast; therefore, it is necessary to look for higher-contrast tools for direct phase measurement.

Motivated by these possibilities, it was shown numerically (and also partly experimentally) that surface plasmonic electron sources can be ideally controlled with ultrashort laser pulses so that they deliver highly directional, monoenergetic electron beams readily synchronized with the pump pulse (Dombi and Rácz, 2008a; Irvine et al., 2004, 2006). We developed a simple semiclassical approach for the simulation of this process analogous to the three-step model of high harmonic generation (Corkum, 1993; Kulander, Schafer, & Krause, 1993). In this chapter, we review the basic elements of this model and prove that it delivers the same results as a much more complicated treatment of the problem based on the rigorous, but computationally time-consuming, solution of Maxwell's equations. Results gained with this latter method showed very good agreement with experimental electron spectra (Irvine, 2006). We also provide new insight into the spatiotemporal dynamics of SPP-enhanced electron acceleration, which is also important if one intends to realize adaptive emission control methods (Aeschlimann et al., 2007).

2. ELECTRON EMISSION AND PHOTOACCELERATION IN SURFACE PLASMON FIELDS

2.1. Emission Mechanisms

Laser-induced electron emission processes of both atoms and solids are determined by the intensity of the exciting laser pulse. At low intensities where the field of the laser pulse is not sufficient to distort the potential significantly, multiphoton-induced processes dominate at visible wavelengths. These nonlinear processes can be described by a perturbative approach in this case. Light-matter interaction is predominantly non-adiabatic and it is governed by the evolution of the amplitude of the laser field, or, in other words, the intensity envelope of the laser pulse.

Tunneling or field emission takes over at higher intensities. This emission regime is determined by the fact that the potential is distorted by the laser field to an extent that it allows tunneling (or, at even higher intensities, above-barrier detachment) of the electron through the modulated potential barrier, the width of which is determined by the laser field strength. The interaction is determined by the instantaneous field strength of the laser pulse; the photocurrent generated in this manner follows the field evolution

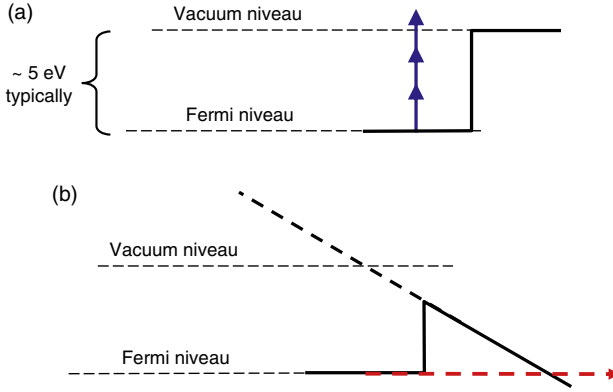


FIGURE 1 Schematic illustration of photo-induced electron emission processes in different laser-intensity regimes when the work function of the metal is more than twice the photon energy (typical for most metals and for near-infrared wavelengths). (a) Multiphoton-induced photoemission. (b) Tunneling or field emission through the potential barrier the width of which is modulated by the laser field.

adiabatically. This interaction type is also referred to as the strong-field regime of nonlinear optics. The difference between multiphoton-induced and field emission is illustrated in [Figure 1](#).

There are, of course, intermediate intensities where the contribution of multiphoton and field emission processes can become comparable. This case is termed as *non-adiabatic tunnel ionization* and its theoretical treatment is considerably more complicated ([Yudin and Ivanov, 2001](#)). It should be mentioned that at significantly higher intensities characteristically different plasma and relativistic effects can also contribute to the light-matter interaction process. This regime, however, is not discussed here.

It follows from simple considerations that the average oscillation energy of an electron in the field of an infinite electromagnetic plane wave is

$$U_p = \frac{e^2 E_l^2}{4m\omega^2}, \quad (1)$$

where the electron charge and rest mass are denoted by e and m , respectively, ω is the angular frequency, and the field strength of the laser field is given by E_l . This quantity is called *ponderomotive potential* in the literature.

The analysis by [Keldysh \(1965\)](#) yielded the perturbation parameter γ , which proved to be an efficient scale parameter to describe bound-free transitions induced by laser fields. Its value is given by

$$\gamma^2 = \frac{W}{2U_p} = \left(\frac{\omega\sqrt{2mW}}{eE_l} \right)^2, \quad (2)$$

where W is the binding energy of the most weakly bound electron in an atom (ionization potential) or the work function of the metal. It can be shown that for the case $\gamma \gg 1$, multiphoton-induced processes dominate. On the other hand, the $\gamma \ll 1$ condition indicates the dominance of field emission. The intensity corresponding to $\gamma \sim 1$ signifies the transition regime between multiphoton-induced and field emission (Farkas, Chin, Galarneau, & Yergeau, 1983; Tóth, Farkas, & Vodopyanov, 1991) and this parameter region is sometimes termed the non-adiabatic tunnel ionization regime (Yudin and Ivanov, 2001). It can also be shown that $\gamma = \tau_t \omega$ holds where τ_t is the Büttiker–Landauer traversal time for tunneling (Büttiker and Landauer, 1982).

2.2. Emission Currents

2.2.1. Multiphoton-Induced Emission

As suggested by the previous considerations, the time dependence of the electron emission currents can be described by different formulas in the multiphoton and the field emission cases. During multiphoton-induced emission the energy of n photons is converted into overcoming the work function of the metal and into the kinetic energy of the freed electron: $n\hbar\omega = E_{\text{kin}} + W$. In this case, the probability of the electron generation is proportional to the n th power of the intensity of the laser field:

$$j(t) \propto I^n(t). \quad (3)$$

This formula yields a very good approximation of the temporal emission profile, provided that no finite-lifetime intermediate states exist. For example, the full quantum mechanical description of the multiphoton-induced photoemission process yielded a very similar dependence recently (Lemell, Tong, Krausz, & Burgdörfer, 2003), although with a somewhat asymmetric temporal profile. Thus, it can be seen that in this case it is the momentary amplitude of the field oscillation that determines the emission probability. As a result of formula (3), for example, if we take a Gaussian laser pulse profile, $I(t)$, the electron emission curve, $j(t)$, has a full width at half maximum (FWHM) that is \sqrt{n} times shorter than the FWHM of the original $I(t)$ curve (Figure 2).

2.2.2. Field or Tunneling Emission

The case of field or tunneling emission can be described by more complex equations. Depending on the model used, several tunneling formulas have

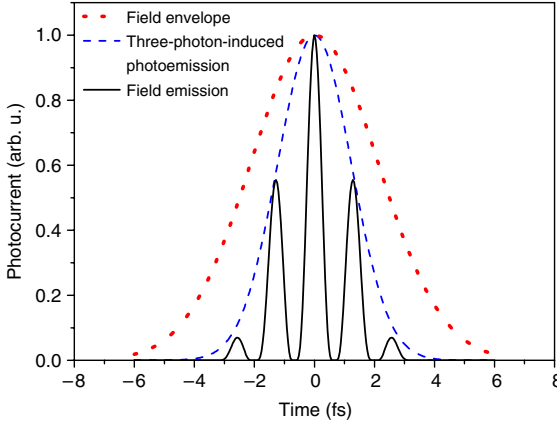


FIGURE 2 Examples of electron emission temporal profiles for a few-cycle laser pulse with a duration of 3.5- fs (intensity full width at half maximum (FWHM)). The dotted curve depicts the field envelope evolution. The dashed curve is the photocurrent temporal distribution for a three-photon-induced photoemission. The solid curve is the photocurrent profile for tunneling electron emission from the surface, determined by the Fowler–Nordheim equation (see text for further details).

been proposed. The one used most generally for metals both for static and for oscillating laser fields is the so-called Fowler–Nordheim equation (Binh, Garcia, & Purcell, 1996; Hommelhoff, Sortais, Aghajani-Talesh, & Kasevich, 2006), where the electric field dependence of the tunneling current is described by

$$j(t) \propto \frac{e^3 E_l(t)^2}{8\pi h W t^2(w)} \exp\left(-\frac{8\pi\sqrt{2m}W^{3/2}}{3he|E_l(t)|}v(w)\right), \quad (4)$$

where $E_l(t)$ denotes the laser field strength, e and m the electron charge and mass, respectively, and h is the Planck constant. W stands for the work function of the metal. $v(w)$ is a slowly varying function taking into account the image force of the tunneling electron with $0.4 < v(w) < 0.8$, and the value of the function $t(w)$ can be taken as $t(w) \approx 1$ for tunneling emission with $w = e^{3/2}\sqrt{E_l/4\pi\epsilon_0}/W$.

The characteristic form of the $j(t)$ curve for this case is shown in Figure 2. The electron emission is concentrated mainly in the vicinity of those instants when the field strength reaches its maximum value. Note that the experimental investigation of pure field emission is very limited for metals (at visible wavelengths) since the damage threshold of bulk metal surfaces and thin films lies around an intensity of 10^{13} W/cm², which is very close to the intensity value where the $\gamma \sim 1$ condition is met. A practical approach

to circumnavigate this problem is needed, to be able to investigate these processes experimentally. The exploitation of far-infrared sources proved suitable for this purpose where the $\gamma \sim 1$ condition can be met at much lower intensities (Farkas et al., 1983). In addition, plasmonic field enhancement can be exploited in the visible spectral region so that $\gamma \ll 1$ can be achieved for metal films without damaging the surface. This latter method is also more advantageous due to the lack of ultrashort laser sources in the far-infrared domain. The phenomenon of plasmonic field enhancement is described in detail in the next section.

2.3. Electron Acceleration in Evanescent Surface Plasmon Fields

After photoemission had taken place from the metal surface, the electrons travel in vacuum dressed by the SPP field. This situation can be approximated by solving the classical equations of motion for the electron in the electromagnetic field of the surface plasmons. This concept is somewhat similar to the three-step model of high harmonic generation on atoms where the electron is considered as a free particle after tunneling photoionization had taken place induced by the electric field of the laser pulse (Corkum, 1993; Kulander et al., 1993). We adapted a model similar to the SPP environment where instead of a single atom, a solid surface is involved that determines the conditions for recollision. Because of the presence of the surface, many electrons recollide or cannot even accelerate because the Lorentz force points toward the surface at the instant of photoemission, or, in other words, at the instant of the "birth" of the electron in vacuum. This latter situation is also modeled by recombination; therefore, these electrons must be disregarded when the properties of the electron bunch are determined.

The rest of the electrons experience cycle-by-cycle kinetic energy gain and become accelerated along the electric field gradient. This mechanism is the same if the envelope of the laser pulse is made up of only few optical cycles; however, the final kinetic energy will not be composed of a large number of incremental, cycle-by-cycle kinetic energy gain portions as in the case of long pulses. Due to the reduced time the electrons spend in the field of the few-cycle SPPs, however, the expected final kinetic energy will be lower. These intuitive predictions are confirmed numerically in the upcoming sections.

3. NUMERICAL METHODS TO MODEL SURFACE PLASMON-ENHANCED ELECTRON ACCELERATION

3.1. Elements of the Model

As discussed previously, SPP-enhanced electron acceleration involves distinct physical processes such as (i) the coupling of the incident light and surface plasmonic electromagnetic fields, (ii) the photoinjection of the electrons into vacuum from the metal layer, and (iii) the subsequent

acceleration of free electrons by the decaying SPP field on the vacuum side of the surface. The elements of the model that we used correspond to these individual steps of the process; therefore, they are presented in separate sections below.

3.1.1. Solution of the Field

In order to determine SPP fields accurately, Maxwell's equations can be solved with the so-called *finite difference time-domain* (FDTD) method. This approach was used for the Kretschmann–Raether SPP coupling configuration in previous studies (Irvine and Elezzabi, 2006; Irvine et al., 2004). In this case, the components of the electric field, the electric displacement, and the magnetic intensity vectors are solved for a grid placed upon the given geometry. Since the FDTD method provides the complete numerical solution of Maxwell's equations, it is computationally rather intensive and more complex geometries cannot be handled with simple personal computers due to the increased processor times required.

Therefore, we proposed analytic formulas to describe SPP fields (Dombi and Rácz, 2008a). Based on the well-known fact that these fields decay exponentially by moving away from the surface (Raether, 1988), we took an analytic expression for the SPP field components on the vacuum side of the metal layer in the form of

$$E_y^{\text{SPP}}(x, y, t) = \eta E_0 E_{\text{env}}(x, t) \cos(k_{\text{SPP}}x - \omega t + \varphi_0) \exp(-\alpha y) \quad (5a)$$

$$E_x^{\text{SPP}}(x, y, t) = \eta a E_0 E_{\text{env}}(x, t) \cos\left(k_{\text{SPP}}x - \omega t - \frac{\pi}{2} + \varphi_0\right) \exp(-\alpha y), \quad (5b)$$

where E_0 is the field amplitude, $E_{\text{env}}(x, t)$ is an envelope function determined by the temporal and spatial beam profiles of the incoming Gaussian pulse, η is the field enhancement factor resulting from plasmon coupling (Raether, 1988), k_{SPP} is the SPP wave vector, ω is the carrier frequency, φ_0 is the CE phase of the laser pulse, and α is the decay length of the plasmonic field in vacuum given by

$$\alpha^{-1} = \sqrt{\frac{\omega^2}{c^2} - k_{\text{SPP}}^2} \quad (6)$$

(Irvine and Elezzabi, 2006). For laser pulses with a central wavelength of 800 nm, the evanescent decay parameter $\alpha = 247 \text{ nm}^{-1}$ follows from Eq. (6). We used the value of $a = 0.3$ according to the notion that the amplitudes of the x - and y -components of the plasmonic field have this ratio according to the numerical solution of Maxwell's equations (Irvine and Elezzabi, 2006). It can be concluded that the field given by Eqs. (5a) and (5b) approximates the exact SPP field with very good accuracy by comparing our results to

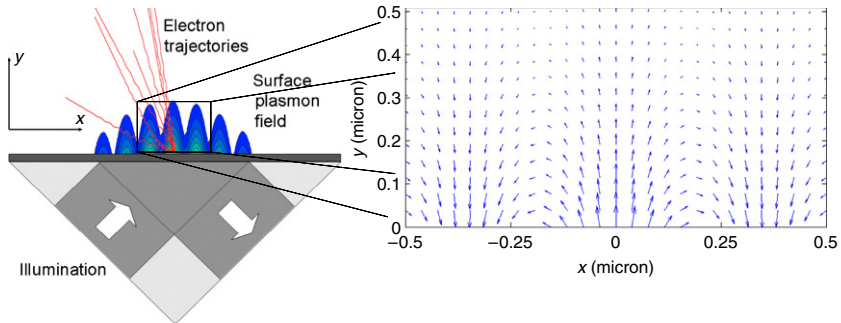


FIGURE 3 Illustration of the setup for the generation of electron beams by surface plasmon-enhanced electron acceleration with the distribution of the electric field amplitude on the vacuum side of the surface, field vectors (inset) and electron trajectories. For further details, see text. (Source: [Dombi and Rácz \(2008a\)](#).)

those of [Irvine and Elezzabi \(2006\)](#). The distribution of the field amplitude in the vicinity of the surface is shown in [Figure 3](#) which shows very good agreement with the above-mentioned calculation. We also succeeded in reproducing the vector representation of the field depicted in [Figure 3](#) of [Irvine and Elezzabi \(2006\)](#) with this method. The representation of the vector field that can be calculated with our model is depicted in the inset of [Figure 3](#).

3.1.2. Electron Emission Channels and Currents Induced by Plasmonic Fields

After the determination of the field, a point array can be placed along the prism surface and the spatial and temporal distribution of the photoemission (induced by the SPP field) along the surface can be examined, assuming that field emission takes place at higher intensities. To this end, we applied the Fowler–Nordheim equation routinely used in studies involving electron emission from metal nanotips ([Hommelhoff, Kealhofer, & Kasevich, 2006](#); [Hommelhoff, Sortais et al., 2006](#); [Ropers, Solli, Schulz, Lienau, & Elsaesser, 2007](#)). This describes the instantaneous tunneling current based on the fact that plasmonic fields carry substantial field enhancement factors (up to $\times 100$) compared to the generating field. One can gain a spatially and temporally resolved map of tunneling probabilities determined by the SPP field this way. The temporal distribution, for example, can be seen in [Figure 2](#). Similar probability distribution curves also result for the spatial coordinates. According to these probabilities, each photoemitted and SPP-accelerated electron that is examined can be assigned a corresponding weight. This weight must be used to accurately determine the final kinetic energy spectrum of the electron beam.

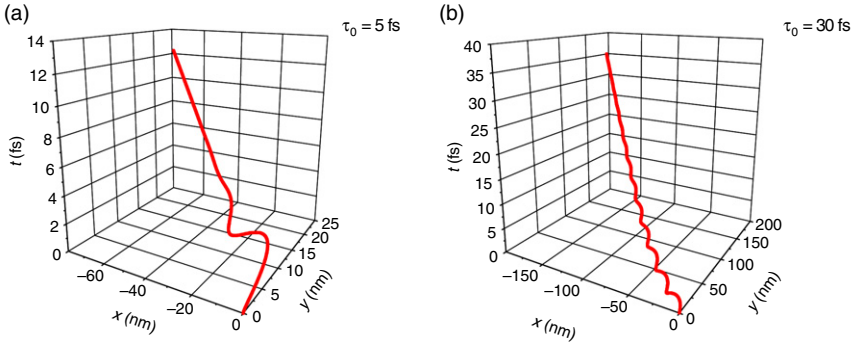


FIGURE 4 Two selected electron trajectories for a 5 fs-long SPP exciting laser pulse (a) and a 30 fs-long pulse (b) illustrating the difference between the few-cycle and the multicycle case. The central wavelength of the laser pulse is 800 nm in both cases. (Courtesy of P. Rácz.)

3.1.3. Particle Acceleration in the Evanescent Field

As a final step in the numerical model, each vacuum electron trajectory of photoemitted electrons in the plasmonic field is investigated for each point in the above-mentioned array and for several emission instants. This is done by solving free-electron equations of motions numerically in the SPP field given by Eqs. (5a) and (5b). Some representative trajectories are shown in Figure 3 (gray curves). Two selected trajectories for 5-fs long exciting pulses (FWHM) as well as for 30-fs long pulses are depicted in Figure 4, illustrating the difference between the acceleration process in the few-cycle and in the multicycle case.

In some cases, the electron trajectories involve a recollision with the metal surface; when this happens, no electron emission is assumed. In all other cases, the final kinetic energies and directions of the photoemitted and photoaccelerated electrons are placed in a matrix for each emission point in space and for each emission instant. Figure 5 illustrates the temporal distribution of the final kinetic energies as a function of the electron “birth” instant for a maximum plasmonic field strength of 5.8×10^{10} V/m and for electrons emitted from the central spot of the illuminated surface in case of a 5-fs long exciting pulse with 800-nm central wavelength. Figure 5 demonstrates similarities to the corresponding kinetic energy distributions of atomic electrons after being accelerated by the ionizing laser field (Reider, 2004). As opposed to that case, it is important to note here that only roughly one-fourth of all emission instants contribute to the acceleration process. This is due to the symmetry breaking of the metal surface and the associated electron recollision and reabsorption processes, as discussed in Section 2.3. Macroscopic emission distributions and electron spectra can be calculated

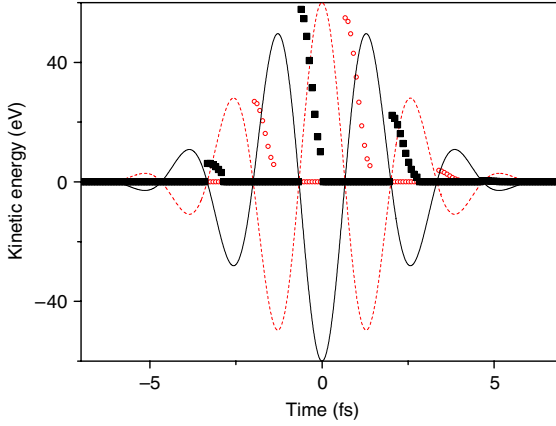


FIGURE 5 Surface plasmon-accelerated electron energy as a function of the birth instant of the electrons (scatterplots). The electric field of the plasmon generating 5-fs laser pulse (illustrated with solid and dashed lines) has either a “cosine” (dashed) or “minus cosine” waveform (solid) under the same envelope. The corresponding electron energies for the cosine waveform are depicted as circles, whereas for the minus cosine waveform as squares. See text for further pulse parameters.

after the assessment of each trajectory by integrating the above-described emission maps along the spatial and/or temporal coordinates.

3.2. Model Results

3.2.1. Electron Acceleration with Multiphoton-Induced Emission

We checked first whether the modeling results reproduce former measurement and simulation spectra (published in Irvine et al. (2004, 2006), Irvine and Elezzabi (2006)) to gain confidence in our simplified 3-step model. To this end, we carried out simulations for the same parameters as those published in these papers. Although for the time being we assume multiphoton-induced electron emission for these simulations (as previously used in these references), we must mention that it does not necessarily hold for higher intensities. However, our purpose in this case was to reproduce former results; therefore, the spatiotemporal distribution of photoemission was described by $j(t, x) \sim I^n(t, x)$, according to Eq. (3). $n = 3$ is used here according to the 4...5 eV work function of most metal surfaces and films and the 1.5 eV photon energy at 800 nm. Figure 6a depicts macroscopic electron spectra gained with our model for peak plasmonic fields of 1.9×10^{11} V/m, 2.7×10^{11} V/m, and 3.7×10^{11} V/m, respectively (the FWHM duration of the input Gaussian laser pulse was 30 fs with a central wavelength of 800 nm). Thereby, this figure can be directly compared with the results in Irvine and Elezzabi (2006), (see Figure 6b). The characteristics

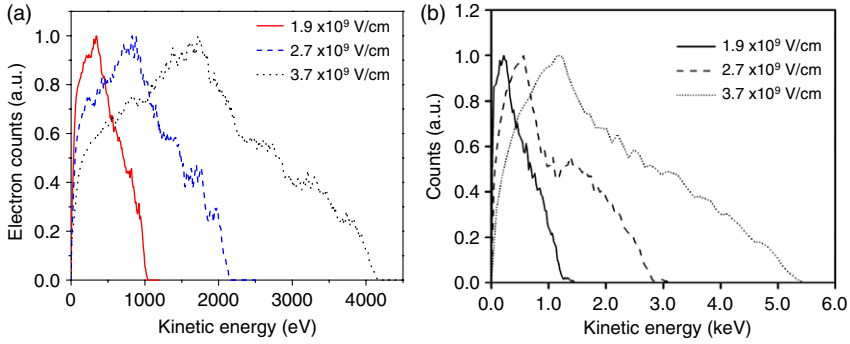


FIGURE 6 (a) Macroscopic electron spectra at peak plasmonic fields of 1.9×10^{11} V/m (solid line), 2.7×10^{11} V/m (dashed line), and 3.7×10^{11} V/m (dotted line) for a Gaussian input laser pulse of 30-fs FWHM duration with a central wavelength of 800 nm. The model used was based on the simplified SPP field description given by Eqs. (5a)–(5b). (b) Electron spectra for the same input parameters with the field calculated with a full FDTD-based simulation. (Source of (b): Irvine and Elezzabi (2006).)

of the electron spectra are very well reproduced, as well as the linear scaling of the kinetic energies of the most energetic electrons with intensity. Slight differences in the peak and cutoff positions can be attributed to the approximate nature of the SPP field expression [Eqs. (5a) and (5b)] used in our case in contrast to the more accurate numerical field solution used by Irvine and Elezzabi (2006).

In another comparative simulation we changed the input pulse length to 5 fs FWHM, and assumed that this pulse is focused to a spot with 60- μm diameter on the prism surface. The field peak was 1.9×10^{11} V/m. Figure 7 shows that the spectrum of the electron beam gained with this approach reproduces the spectrum computed with other methods, such as the one in Irvine and Elezzabi (2006) (depicted with a dashed curve in Figure 7). Slight differences in the cutoff positions can still be observed; however, all spectral features and the position of the main peak are exactly the same. Thus, the applicability of analytic field expressions [Eqs. (5a) and (5b)] and the robustness of our approach are confirmed by these examples.

3.2.2. Electron Acceleration with Field Emission

We now turn our attention to modeling electron spectra by assuming field emission from the metal surface, which is a more realistic assumption for higher-intensity input beams, approaching the damage threshold of thin metal films. The experimental motivation of this study is driven by the fact that high-repetition-rate, ultrafast laser output delivering focused intensity in this range is achievable with simple titanium:sapphire oscillators with an extended cavity, as we demonstrated recently (Dombi and Antal, 2007;

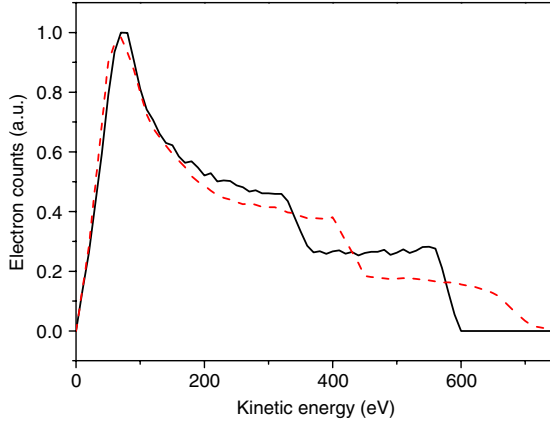


FIGURE 7 Electron spectrum for a 5-fs generating pulse with a peak plasmonic field strength of 1.9×10^{11} V/m, assuming multiphoton photoemission calculated with simplified numerical methods (solid curve) and electron spectrum for the same input parameters with the electric field calculated with a full FDTD-based simulation (source for dashed curve: [Irvine and Elezzabi \(2006\)](#)). See text for further details.

[Dombi, Antal, Fekete, Szipöcs, & Várallyay, 2007](#); [Naumov et al., 2005](#)). We then used the Fowler–Nordheim formula, as given by Eq. (4) and resolved the photoaccelerated electron beam both angularly and spectrally, assuming a maximum input field of 5.8×10^{10} V/m, which is a rather realistic maximum value considering the damage threshold of gold and silver films. We also assumed a tunneling time of 600 attoseconds which, in our model, describes the delay between the actual distortion of the potential by the field and the corresponding appearance of the electron in the continuum.

Several emission maps are presented in the following text, using realistic parameters to reveal the fine structure of the acceleration process and to search conclusions about macroscopically observable properties of the electron beams generated. We examined the final kinetic energy distribution of SPP-accelerated electrons along the plasmon propagation direction (x -axis, representing emission locations along the surface) for a few-cycle interacting pulse with a Gaussian pulse shape, 15-fs and 5-fs intensity FWHM, $\varphi_0 = 0$ CE phase (which means that envelope and field maxima coincide). The central wavelength was 800 nm. The pulse was assumed to be focussed on a spot with a diameter of 4 μm on the prism surface so that a peak plasmon field strength of 5.8×10^8 V/cm (Keldysh-gamma of 0.31) was reached. With this effective intensity value we have already taken into account that substantial field enhancement factors (up to $\times 100$) can be achieved with respect to the SPP generating field.

The spatial and spectral distribution of the emitted electrons along the plasmon propagation direction was calculated with these simulation

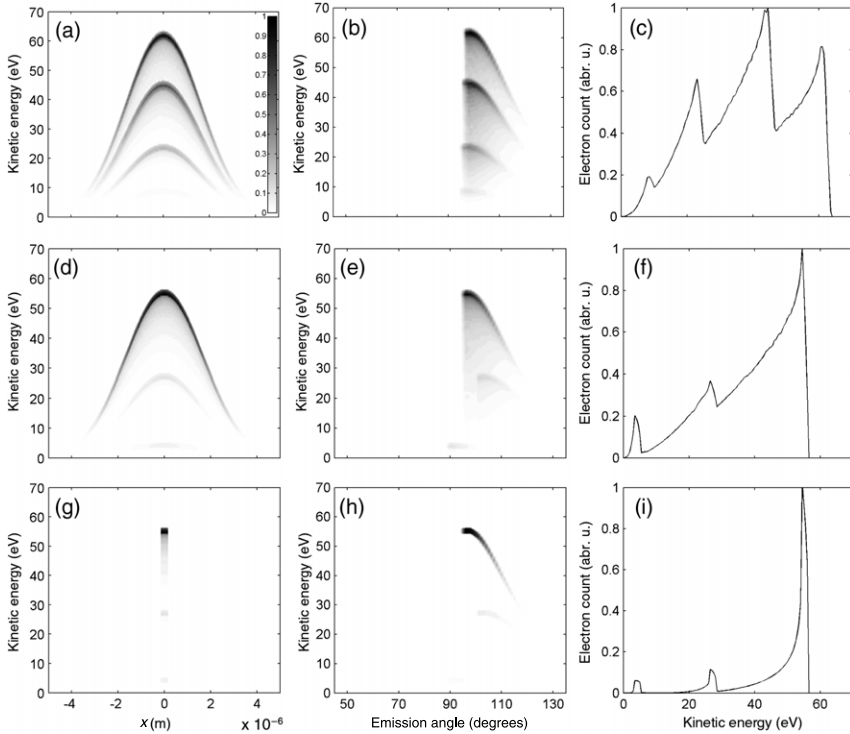


FIGURE 8 Normalized photoacceleration maps (kinetic energy distribution of electrons emitted at different points of the surface: (a), (d) and (g), in grayscale representation); angular and kinetic energy distribution ((b), (e) and (h)); and macroscopic electron spectra ((c), (f), and (i)) of surface plasmon-accelerated electrons for three example parameter sets. Panels (a)–(c) are for 15-fs and (d)–(i) are for 5-fs laser pulses. In panels (g)–(i) we restricted the emission to a spot with 300-nm radius, as illustrated in (g). We modeled a nanolocalized emission region with this approach. See text for further details. (Source: [Dombi and Rácz \(2008a\)](#).)

parameters (in false color representation in [Figures 8a](#) and [d](#)) for two different pulse lengths to illustrate few-cycle effects. Whereas in the multicycle regime (15-fs pulse length) in [Figure 8a](#) a much more structured distribution can be observed, in [Figure 8d](#) (5-fs pulse length) the emission is concentrated primarily at a single structure on the emission map providing a better-behaved electron beam. It can also be seen that the emission of high-energy electrons is localized to the center of the illuminated spot and that the number of distinct structures on the emission maps roughly correspond to the number of optical cycles in the generating pulse. This is because the “birth” interval of those electrons in the continuum that can leave the vicinity of the surface is limited to about one-fourth of every laser cycle. This is due to the breaking of the symmetry by the surface such that positive and negative

half-cycles are not identical from this point of view. Every laser cycle has one such favored interval and electrons emitted in each of these intervals spend different amounts of time in the field; hence, they undergo different acceleration.

An even more conspicuous property seems crucially important from the point of view of the applications of this electron source. Figure 8b and 8e depict the angular-kinetic energy distributions of the emitted electron beams, showing the direction in which the energetic electrons leave the surface. The emission is confined to a small range of angles supporting a directionally emitted electron beam ideally suited for novel ultrafast techniques. Provided that the pulse length is in the few-cycle range (Figure 8e), the angular emission map is reduced to a single distinct structure corresponding to a highly directional, quasi-monoenergetic electron beam representing the most favorable regime of SPP-enhanced electron acceleration. By integrating any of the distributions along the x -axis we derive the macroscopically observable electron spectra depicted in Figures 8c and f. The spectrum in Figure 8f has a FWHM $\Delta E_{\text{kin}}/E_{\text{kin}}$ value of 0.22 (with E_{kin} denoting the electron kinetic energy) corresponding to a quasi-monoenergetic spectrum. The spectral properties of this electron beam can be further enhanced under experimental circumstances by applying a retarding potential to suppress the low-energy wing of the spectrum.

The integrated spectra in Figures 8c, f, and i show a significant difference compared with the one in Figure 7a. This can be attributed exclusively to the different emission regimes (multiphoton vs. tunneling) involved. The sharp temporal distribution of the tunneling peaks located at the field maxima favor the emission of electrons at those time instants when they can gain significant kinetic energy. The sharp spectral cutoff is at the same location as the highest-energy electrons are located in the multiphoton case; however, it is primarily these high-energy electrons that are represented in the field emission case; therefore, a sharp peak appears in the spectrum.

On the other hand, the low-energy wings of the spectra in Figures 8c and f display a broader feature, making the source less suitable for ultrafast applications. To generate spectra with higher monoenergeticity, we suggest the application of spatial confinement of the emission area on the metal surface. This can be carried out experimentally by various nanofabrication techniques — for example, by depositing a dielectric layer on top of the metal with a nanoscale opening where the dielectric overlayer is absent and the metal surface is exposed to vacuum. Another possibility is roughening a small rectangular area on top of the metal surface, thereby enhancing the emission from that portion of the film. These potential schemes were taken into account in our simulations by selecting only smaller areas of the surface illuminated by the laser beam, and we considered only those photoelectrons that were emitted from this area. Results are shown in Figures 8g–i where the same emission maps and spectra are given as in Figures 8d–f with

the only difference that electrons coming only from a 300-nm wide central portion of the surface were considered. By so confining the emission area, the distribution in Figure 8h shows a highly enhanced contrast. This means that even more monoenergetic spectra and even more directional beams can be generated from this spatially confined source. The $\Delta E_{\text{kin}}/E_{\text{kin}}$ value of the integrated spectrum can be enhanced by almost an order of magnitude to 0.033 (see Figure 8i). Our results suggest that SP electron acceleration offers a robust and powerful technique for the generation of ultrafast, monoenergetic, highly directional electron beams (Dombi and Rácz, 2008a).

4. EXPERIMENTAL RESULTS

4.1. Surface Plasmon-Enhanced Photoemission

It is well known that the efficiency of several light-matter interaction phenomena and applications, such as Raman scattering, plasmonic biosensors (Lal, Link, & Halas, 2007), and references therein), surface harmonic generation (Quail, Rako, Simon, & Deck, 1983; Simon, Mitchell, & Watson, 1974), and other surface physical and chemical processes can be significantly enhanced by the roughness of the metal surface involved. It was recently shown that even high harmonic generation on atoms is possible in the vicinity of tailored, nanostructured metal surfaces with the help of this phenomenon (Kim et al., 2008). It was shown that the common reason for the increased effects in most such cases is mainly the field enhancement and SPP coupling due to the roughness of the metal surface involved. It is known that the incident electromagnetic field can be enhanced by a factor of up to $\times 100$ (Raether, 1988) on a rough surface if SPPs are also coupled. This means an enhancement of 10^4 in intensity, which corresponds to a 10^8 enhancement in two-photon photoemission yield according to Eq. (3) in this favorable case. Moreover, even if the surface of a thin metal film is perfectly (atomically) flat, SPP coupling in the Kretschmann–Raether configuration results in a factor of $\times 3 \dots 4$ field enhancement alone at the metal-vacuum interface with respect to the field of the incident beam (Raether, 1988). Even this effect means a drastic photoemission yield enhancement for a perturbative n -photon process.

Therefore, one of the first examples of newly discovered femtosecond surface plasmon-enhanced phenomena was SPP-induced photoemission from metal surfaces (Tsang, Srinivasan-Rao, & Fischer, 1990). More systematic studies with Au, Ag, Cu, and Al surfaces revealed photoemission yield enhancement factors of $\times 50$ to $\times 3500$, which indicate field enhancement values of $\times 2 \dots \times 8$ suggesting that the surfaces involved were of relatively good surface quality (Tsang et al., 1991). Figure 9 shows the main results of these experiments. The curves show the intensity dependence of the photoelectron yield on double logarithmic scales. Therefore, the slope of

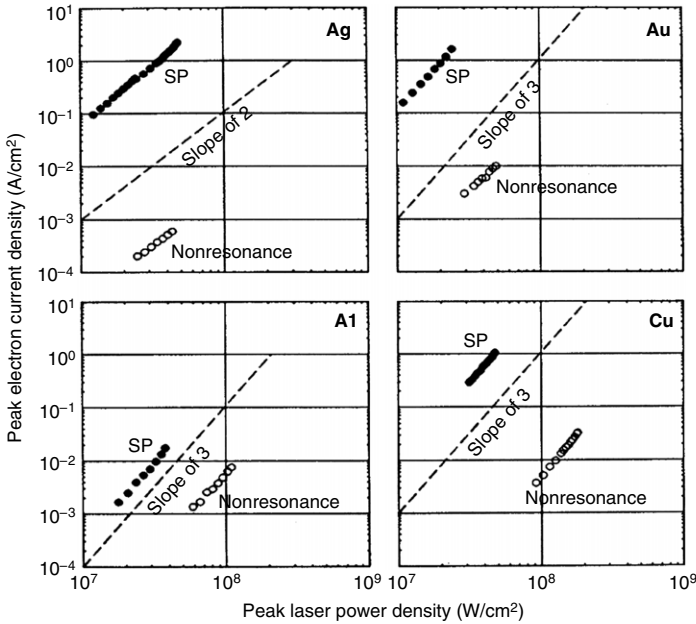


FIGURE 9 The enhancement of SPP-induced multiphoton photoemission yield as a function of the intensity of the incident laser beam for four different surfaces plotted on double logarithmic scales. The slope of each linear fit equals the nonlinearity of the photoemission process. The lower data sets marked as “nonresonance” depict photoelectron yield from the same metal film without SPP coupling but with a similar illumination geometry. The substantial increase of the SPP-enhanced photoelectron yield is clearly illustrated with the upper curves plotted with solid symbols and marked with “SP”. (Source: Tsang et al. (1991)).

each linear fit equals the nonlinearity of the photoemission process. In each case, multiphoton-induced emission takes place since there is no deviation from the linear fits. Moreover, the enhancement of the SPP-enhanced photoelectron yield is illustrated compared with nonlinear photoemission induced from the same film without SPP coupling. These first pioneering results paved the way toward SPP-mediated electron acceleration. Later independent experiments confirmed these results (Chen, Boneberg, & Leiderer, 1993; Irvine et al., 2004).

The fact that the electron yield is much higher if SPP coupling takes place than the yield at direct surface illumination without SPP coupling underscores a very important feature of SPP-enhanced emission processes. Namely, it can be stated that the SPPs induce the observed photocurrent primarily; therefore, it would be more appropriate to term the *multiphoton-induced emission* picture in this case as *multiplasmon-induced* electron emission. Accordingly, it is the enhanced SPP field that distorts the surface

potential in the field emission picture and lowers the tunneling barrier. This means that the field emission regime can be reached at much lower laser input intensities and strong-field phenomena can be induced with high-repetition-rate, cost-effective laser oscillators (see, e.g., [Dombi and Antal, 2007](#); [Dombi et al., 2007](#); [Naumov et al., 2005](#)).

4.2. Generation of High-Energy Electrons

In addition to their enhancement of photoemission yield, SPP fields can also accelerate the electrons that are set free from the surface, thanks to the mechanisms described in Section 2.1. Recently performed spectrally resolved measurements of SPP photoemission delivered the experimental confirmation of this powerful particle acceleration mechanism in evanescent plasmonic fields ([Irvine et al., 2004](#); [Kuperszytch et al., 2001](#); [Zawadzka, Jaroszynski, Carey, & Wynne, 2000](#); [Zawadzka et al., 2001](#)). The main features of these electron spectra, especially the scaling of cutoff energies resulting from this mechanism, could be explained within the framework of the semi-classical three-step model described in Section 3.1 ([Irvine, 2006](#)).

To describe these experiments in detail, [Zawadzka et al.](#) demonstrated SPP-enhanced electron spectra stretching until 400 eV with 40 TW/cm² focused intensity in the Kretschmann SPP coupling configuration. The pulse length was 100–150 fs in that case ([Zawadzka et al., 2000, 2001](#)). [Kuperszytch et al.](#) also showed this phenomenon with laser pulses that were 60-fs long and reached 8 GW/cm² focused intensity ([Kuperszytch et al., 2001](#)). The highest electron energy was ~40 eV in their experiments. SPPs were coupled on a grating surface, and in contrast to the results of [Zawadzka et al.](#), they possessed a peak at higher energies.

[Irvine et al.](#) demonstrated even more conspicuous results in 2004 by accelerating electrons in SPP fields up to 400 eV with a simple titanium:sapphire oscillator delivering merely 1.5-nJ pulse energy. The resulting focused intensity was 1.8 GW/cm². Most interestingly, the SPP-enhanced electron spectrum became quasi-monoenergetic peaking at 300 eV with a FWHM of 83 eV ([Figure 10](#)).

The increased enhancement and confined electron emission in the latter experiment can be explained by considering the surface morphology of the silver film. Surface roughness effects alter the spatial distribution of the SPP field on a nanometer scale (<50 nm) and are not included in the FDTD-based model calculations ([Irvine et al., 2004](#)). In such cases, the overall energy of the pulse is conserved, but the energy density is drastically increased by confinement of the radiation to sub-wavelength volumes and is manifested as an additional localized electric field enhancement. This explanation is further supported by the fact that the modeled electron emission had to be restricted to within 10% of the laser spot ([Figure 10](#)) to enable the reproduction of measurement results. Due to the highly nonlinear photoemission, small peaks or protrusions at the metal surface would

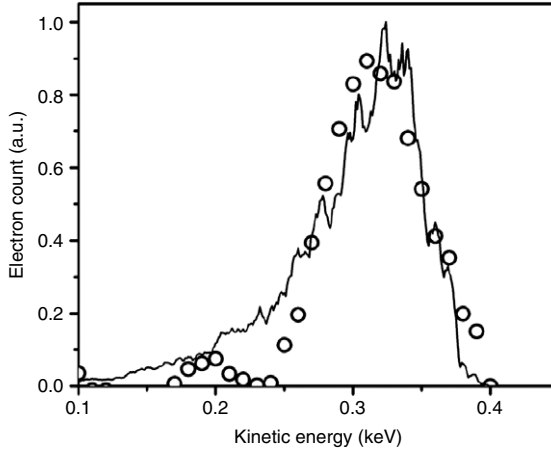


FIGURE 10 Comparison between a measured electron energy spectrum using a Ti-sapphire laser oscillator (circles) and theoretical energy spectra (solid line) as calculated from an FDTD-based model. (Source: [Irvine \(2006\)](#).)

dominate the electron emission in the presence of an SPP wave, and it would appear that electrons originate only from such defects with a reduced spatial extent. A full account of surface roughness necessitates three-dimensional FDTD calculation, which over the length scales of electron emission and acceleration, requires enormous computational effort. Nevertheless, the principal effects underlying efficient SPP-enhanced acceleration can be seen from these initial, approximate simulations.

The same authors also demonstrated acceleration up to 2 keV recently by applying higher-intensity laser pulses with the help of an amplified titanium:sapphire laser system, delivering proof of the scalability of the electron acceleration process with laser intensity ([Irvine and Elezzabi, 2005](#)).

In summary, spectrally resolved measurements confirmed that SPP-enhanced electron acceleration is a very powerful method to generate multi-kiloelectronvolt electron beams with high-repetition-rate, low-intensity laser pulses. Simple scaling laws, such as the linear scaling of the highest electron energies with the incident laser intensity, were confirmed in these measurements. Since a great variety of different spectral shapes were observed in these pioneering studies, more systematic experiments are needed to establish the optimum focusing conditions and coating methods (surface morphologies) to enable the generation of well-behaved, high-energy, monoenergetic beams.

4.3. Time-Resolved Studies of the Emission

By combining optical pump-probe methods with surface science techniques, time-resolved studies can be performed on photoemission processes from

thin metal films. The most widespread example of such an experimental scheme is recording the autocorrelation functions using multiphoton-induced emission or surface harmonic generation processes acting as nonlinear “detectors” instead of the standard second harmonic generation scheme with nonlinear crystals (Melnikov, Povolotskiy, & Bovensiepen, 2008; Moore and Donnelly, 1999; Petek and Ogawa, 1997).

The implementation of this technique in this particular case is the recording of the SPP-enhanced photoemission signal as a function of the delay between the ultrashort-pulse replicas produced by a Michelson interferometer and extracting information on the evolution and characteristic time scales of the surface process by means of deconvolution. This method was applied particularly successfully in case of two-photon photoemission phenomena from metals and surface adsorbates (Petek and Ogawa, 1997, and references therein). With the rapid development of femtosecond laser technology, such methods were recently extended to the few-cycle domain, too (Dombi, Krausz, & Farkas, 2006). The interferometric or the background-free autocorrelation functions that can be measured this way provide indirect information on the lifetime of any potential intermediate states the electrons undergo during photoemission (Georges and Karatzas, 2008), optical excitation of hot electrons (Petek and Ogawa, 1997), image potential effects (Schoenlein, Fujimoto, Eesley, & Capeherat, 1988), and so forth.

Time-resolved characterization in case of SPP-induced photoemission was carried out by several groups to gain insight into ultrafast emission dynamics of this process on pico- and femtosecond time scales (Chen et al., 1993; Irvine et al., 2004; Kupersztych et al., 2001; Tsang et al., 1991). The higher-order autocorrelation traces revealed in each case that the electron pulse length is roughly $n^{1/2}$ times shorter than that of the exciting laser pulse, where n is the order of the photoemission process ($n = 2, \dots, 4$ in these experiments). Therefore, the temporal profile of the electron bunch can be well approximated with Eq. (3). As can be seen from the comparison of these articles, this holds for a very broad range of pulse durations since such a behavior was observed both for nanosecond-long exciting pulses (Chen et al., 1993), as well as for femtosecond excitation (Irvine et al., 2004) where pulses of 27-fs duration were used. For example, the third-order interferometric autocorrelation trace measured with three-photon-induced, SPP-enhanced photoemission in the latter case is depicted in Figure 11.

These results suggest that the influence of surface states and hot electron excitation is negligible on the time scales that were examined, and the photoemission process can be considered instantaneous with respect to the intensity evolution of the exciting laser pulse in the material environments that were considered (mostly polycrystalline, evaporated Ag and Au thin films). Unfortunately, compared with the wealth of measurements conducted with the two-photon photoemission technique on ultrafast dynamics at

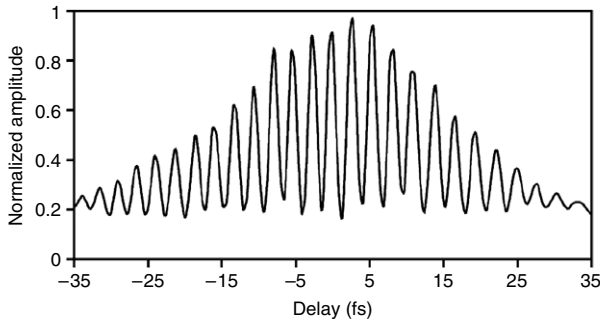


FIGURE 11 Measured interferometric two-pulse three-photon photoemission correlation trace for 27-fs laser pulses, indicating that at the surface of the film, the electron pulse duration is less than 27 fs (Source: [Irvine et al. \(2004\)](#).)

metal surfaces ([Petek and Ogawa, 1997](#)), there are significantly fewer data for time-resolved measurements of SPP-enhanced electron acceleration. These measurements also lack in-depth evaluation and thus further studies are needed to establish the underlying processes in the ultrafast dynamics of this phenomenon. Nevertheless, these initial studies carry a very important positive message. The ultrashort nature of these electron bunches upon leaving the surface indicates that the SPP-enhanced electron acceleration effect can be particularly well implemented in the development of novel ultrafast time-resolved methods where electron pulses of few-femtosecond duration are required.

5. THE ROLE OF THE CARRIER-ENVELOPE PHASE

5.1. Light-Matter Interaction with Few-Cycle Laser Pulses, Carrier-Envelope Phase Dependence

Optical waveform control of recollision processes of atomic electrons had brought deeper insight into atomic physics since the reproducible generation of attosecond light pulses in gas targets was enabled by CE phase control of few-cycle light pulses (see, e.g., ([Agostini and Dimauro, 2004](#)), and references therein). Similarly, in solids, the CE phase played a decisive role in governing various charge transfer and photoemission processes, as measured with the first CE phase-stabilized oscillators ([Apolonski et al., 2004](#); [Dombi and Rácz, 2008b](#); [Dombi et al., 2004](#); [Fortier et al., 2004](#); [Mücke et al., 2004](#)). These experiments revealed several new aspects of the underlying light-matter interaction physics, even though the underlying mechanisms by many of these processes are not fully understood and there is substantial discrepancy between various semiclassical and quantum mechanical models and measured results ([Dombi et al., 2004](#); [Lemell et al., 2003](#)).

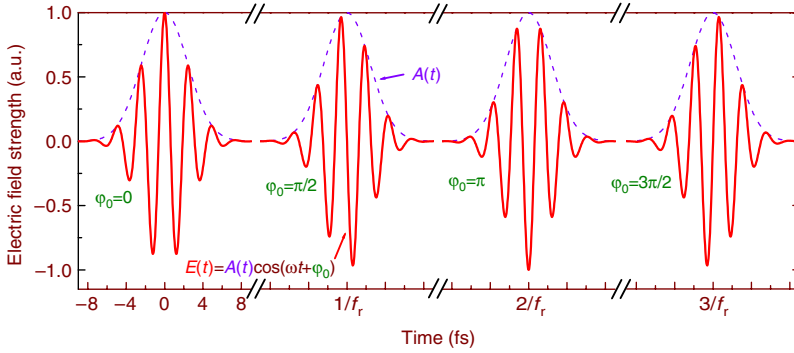


FIGURE 12 Few-cycle laser pulses with different CE phase values representing different optical waveforms (solid line) under the same field envelope (dashed line). ($\tau_L = 4$ fs, $\lambda_0 = 750$ nm, Gaussian pulse shape: $A(t) = A_0 \exp(-2t^2 \ln 2 / \tau_L^2)$.)

The optical waveform of a transform-limited ultrashort laser pulse can be parameterized with the CE phase value for a given envelope shape. An arbitrary, chirp-free laser pulse shape can be defined by the equation

$$E_I(t) = A(t) \cos(\omega t + \varphi_0), \quad (7)$$

where $A(t)$ is the field envelope and ω is the central angular frequency of the laser and φ_0 is the CE phase. Depending on the value of φ_0 , significantly different optical waveforms can occur provided that the pulse length is in the few-cycle domain. This is illustrated in Figure 12 where different waveforms are depicted under the same Gaussian envelope.

The self-referencing or f -to- $2f$ technique allows control of CE phase evolution in the typically multi-megahertz train of pulses by stabilizing $\Delta\varphi_0$ (i.e., the pulse-to-pulse CE phase shift in the output of a mode-locked laser) (Jones et al., 2000). State-of-the-art laser systems were developed in past years by exploiting this novel optical technology. These delivered CE phase-stabilized pulses as short as 3.7 fs (Yakovlev et al., 2003). However, an f -to- $2f$ interferometer usually used in these schemes is not suitable for measuring the absolute value of φ_0 ; only the pulse-to-pulse CE phase shift value ($\Delta\varphi_0$) can be stabilized. Despite this shortcoming, basic experiments could be done with these types of lasers demonstrating the effect of the optical waveform on laser-solid interactions (Apolonski et al., 2004; Dombi and Rácz, 2008b; Dombi et al., 2004; Fortier et al., 2004; Mücke et al., 2004).

5.2. Carrier-Envelope Phase-Controlled Electron Acceleration

Motivated by these developments, we examined the effect of the optical waveform on the electron beam generated in this parameter regime

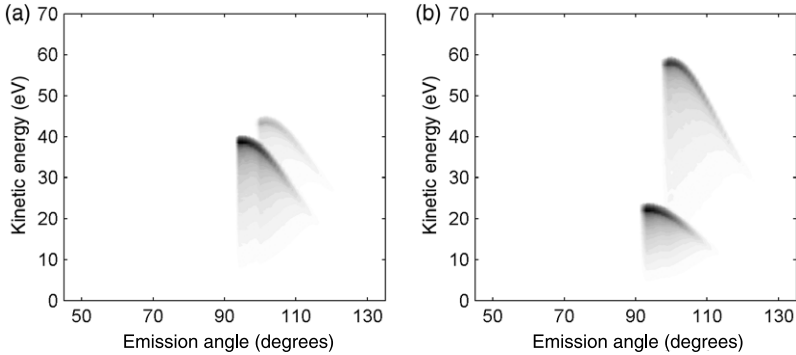


FIGURE 13 Angle-energy distributions of SPP-enhanced photoacceleration for carrier-envelope-phase values of (a) $\pi/2$ and (b) π . Other than the CE phase value, the simulation parameters were the same as those used to calculate Figure 8e. These distributions can be directly compared to Figure 8e, where the CE phase value was $\varphi_0 = 0$. (Source: Dombi and Rácz (2008a).)

numerically (Dombi and Rácz, 2008a). The angle-energy distributions in Figures 13a and b (CE phases of $\pi/2$ and π , respectively) can be directly compared to that of Figure 8e (CE phase $\varphi_0 = 0$); the only difference in the simulation input is that we varied the CE phase of the interacting pulses but otherwise left other parameters unchanged. We can see that the spectral cutoffs determined by the acceleration process are highly dependent on the CE phase of the pulses in accordance with previous results (Irvine and Elezzabi, 2006). In our case, however, by having taken tunneling emission into account (instead of multiphoton emission) the influence of the CE phase becomes more pronounced. The number of structures observable on the emission maps corresponds to the number of optical cycles in the laser pulse (two in this case). These structures coincide for CE phase values of 1.75π and $\pi/4$ serving as a basis for an ideal photoelectron source. Therefore, it is anticipated that the generation of electron beams with the desired spatial, spectral, and temporal features requires femtosecond laser sources with CE phase stabilization. The experimental verification of these predictions can be carried out with state-of-the-art few-cycle laser sources.

6. CONCLUSIONS

In conclusion, SPP-enhanced electron acceleration proved to be a powerful method for the all-optical generation of ultrashort, high-repetition-rate electron beams with kiloelectronvolt-range energy. The initial duration of these electron bunches is limited by the width of the envelope function of the laser pulse, and in the case of high-order multiphoton-induced processes it can be significantly shorter than the FWHM of the femtosecond

optical excitation. The properties of these electron beams can be sensitively tuned with the parameters of the SPP exciting laser pulse, such as the intensity, focusing, pulse shape, or the CE phase, demonstrating a full coherent control perspective in a solid-state system. In addition, the field enhancement intrinsic to SPPs enables the investigation of a wealth of strong-field phenomena in surface environments. SPP coupling together with surface nanostructures hold promise of circumventing the damage threshold problem related to surfaces, which is the main obstacle to strong-field light-matter interaction experiments in solid environments. Thus, SPP-enhanced photoemission and photoacceleration processes as versatile tools will open the door to novel surface characterization, ultrafast, spatially resolved pump-probe methods and to strong-field plasmonics in the future.

ACKNOWLEDGMENTS

The author received support from the Hungarian Scientific Research Fund (OTKA Project F60256). The author was also supported by the Bolyai Fellowship of the Hungarian Academy of Sciences. Fruitful discussions with Gyözö Farkas and the help of Péter RÁCZ in the preparation of the figures are gratefully acknowledged.

REFERENCES

- Aeschlimann, M., Bauer, M., Bayer, D., Brixner, T., García de Abajo, F. J., Pfeiffer, W., et al. (2007). Adaptive subwavelength control of nano-optical fields. *Nature*, *446*, 301–304.
- Agostini, P., & Dimauro, L. F. (2004). The physics of attosecond light pulses. *Rep. Prog. Phys.*, *67*, 813–855.
- Apolonski, A., Dombi, P., Paulus, G. G., Kakehata, M., Holzwarth, R., Udem, T., et al. (2004). Observation of light-phase-sensitive photoemission from a metal. *Physical Review Letters*, *92*, 073902.
- Binh, V. T., Garcia, N., & Purcell, S. T. (1996). Electron field emission from atom-sources: fabrication, properties, and applications of nanotips. *Advances in Imaging Electron Physics*, *95*, 63.
- Büttiker, M., & Landauer, R. (1982). Traversal time for tunnelling. *Physical Review Letters*, *49*, 1739–1742.
- Chen, H., Boneberg, J., & Leiderer, P. (1993). Surface-plasmon-enhanced multiple-photon photoemission from Ag and Al films. *Physical Review Letters*, *47*, 9956–9958.
- Corkum, P. B. (1993). Plasma perspective of strong-field multiphoton ionization. *Physical Review Letters*, *71*, 1994–1997.
- Dombi, P., & Antal, P. (2007). Investigation of a 200 nJ Ti:sapphire oscillator for white light generation. *Laser Phys. Lett.*, *4*, 538–542.
- Dombi, P., & RÁCZ, P. (2008a). Ultrafast monoenergetic electron source by optical waveform control of surface plasmons. *Optics Express*, *16*, 2887–2893.
- Dombi, P., & RÁCZ, P. (2008b). Carrier-envelope phase-controlled laser-surface interactions. *Proceedings of SPIE*, *6892*, 68921J.
- Dombi, P., Krausz, F., & Farkas, G. (2006). Ultrafast dynamics and carrier-envelope phase sensitivity of multiphoton photoemission from metal surfaces. *Journal of Modern Optics*, *53*, 163–172.

- Dombi, P., Apolonski, A., Lemell, C., Paulus, G. G., Kakehata, M., Holzwarth, R., et al. (2004). Direct measurement and analysis of the carrier-envelope phase in light pulses approaching the single-cycle regime. *New Journal of Physics*, 6, 39.
- Dombi, P., Antal, P., Fekete, J., Szipöcs, R., & Várallyay, Z. (2007). Chirped-pulse supercontinuum generation with a long-cavity Ti:sapphire oscillator. *Applied Physics B*, 88, 379–384.
- Farkas, G., Chin, S. L., Galarneau, P., & Yergeau, F. (1983). *Optics Communications*, 48, 275–278.
- Fill, E., Veisz, L., Apolonski, A., & Krausz, F. (2006). Sub-fs electron pulses for ultrafast electron diffraction. *New Journal of Physics*, 8, 272.
- Fortier, T. M., Roos, P. A., Jones, D. J., Cundiff, S. T., Bhat, R. D. R., & Sipe, J. E. (2004). Carrier-envelope phase-controlled quantum interference of injected photocurrents in semiconductors. *Physical Review Letters*, 92, 147403.
- Georges, A. T., & Karatzas, N. E. (2008). Modeling of ultrafast interferometric three-photon photoemission from a metal surface irradiated with sub-10-fs laser pulses. *Physical Review B*, 77, 085436.
- Hommelhoff, P., Kealhofer, C., & Kasevich, M. A. (2006). Ultrafast electron pulses from a tungsten tip triggered by low-power femtosecond laser pulses. *Physical Review Letters*, 97, 247402.
- Hommelhoff, P., Sortais, Y., Aghajani-Talesh, A., & Kasevich, M. A. (2006). Field emission tip as a nanometer source of free electron femtosecond pulses. *Physical Review Letters*, 96, 077401.
- Irvine, S.E. (2006). Laser-field femtosecond electron pulse generation using surface plasmons. Doctoral thesis, University of Alberta, Canada.
- Irvine, S. E., & Elezzabi, A. Y. (2005). Ponderomotive electron acceleration using surface plasmon waves excited with femtosecond laser pulses. *Applied Physics Letters*, 86, 264102.
- Irvine, S. E., & Elezzabi, A. Y. (2006). Surface-plasmon-based electron acceleration. *Physical Review A*, 73, 013815.
- Irvine, S. E., Dechant, A., & Elezzabi, A. Y. (2004). Generation of 0.4-keV femtosecond electron pulses using impulsively excited surface plasmons. *Physical Review Letters*, 93, 184801.
- Irvine, S. E., Dombi, P., Farkas, G., & Elezzabi, A. Y. (2006). Influence of the carrier-envelope phase of few-cycle pulses on ponderomotive surface-plasmon electron acceleration. *Physical Review Letters*, 97, 146801.
- Jones, D. J., Diddams, S. A., Ranka, J. K., Stentz, A., Windeler, R. S., Hall, J. L., et al. (2000). Carrier-envelope phase control of femtosecond mode-locked lasers and direct optical frequency synthesis. *Science*, 288, 635–639.
- Keldysh, L. V. (1965). Ionization in the field of a strong electromagnetic wave. *Soviet Physics - Journal of Experimental and Theoretical Physics*, 20, 1307.
- Kim, S., Jin, J., Kim, Y.-J., Park, I.-J., Kim, Y., & Kim, S.-W. (2008). High-harmonic generation by resonant plasmon field enhancement. *Nature*, 453, 757–760.
- Kulander, K. C., Schafer, K. J., & Krause, J. L. (1993). Dynamics of short-pulse excitation, ionization and harmonic conversion. In B. Piraux (Ed.), *Proc. workshop super intense laser atom physics (SILAP III)* (p. 95). New York: Plenum.
- Kupersztych, J., Monchicourt, P., & Raynaud, M. (2001). Ponderomotive acceleration of photoelectrons in surface-plasmon-assisted multiphoton photoelectric emission. *Physical Review Letters*, 86, 5180–5183.
- Lal, S., Link, S., & Halas, N. J. (2007). Nano-optics from sensing to waveguiding. *Nature Photonics*, 1, 641–648.
- Leemans, W. P., Nagler, B., Gonsalves, A. J., Tóth, Cs., Nakamura, K., Geddes, C. G. R., et al. (2006). GeV electron beams from a centimetre-scale accelerator. *Nature Physics*, 10, 696–699.
- Lemell, C., Tong, X.-M., Krausz, F., & Burgdörfer, J. (2003). Electron emission from metal surfaces by ultrashort pulses: Determination of the carrier-envelope phase. *Physical Review Letters*, 90, 076403.
- Lobastov, V. A., Srinivasan, R., & Zewail, A. H. (2005). Four-dimensional ultrafast electron microscopy. *Proceedings of National Academy of Sciences*, 102, 7069–7073.
- Melnikov, A., Povolotskiy, A., & Bovensiepen, U. (2008). Magnon-enhanced phonon damping at Gd(0001) and Tb(0001) surfaces using femtosecond time-resolved optical second-harmonic generation. *Physical Review Letters*, 100, 247401.

Author's personal copy

- Moore, K. L., & Donnelly, T. D. (1999). Probing nonequilibrium electron distributions in gold by use of second-harmonic generation. *Optics Letters*, *24*, 990–992.
- Mücke, O. D., Tritschler, T., Wegener, M., Morgner, U., Kärtner, F. X., Khitrova, G., et al. (2004). Carrier-wave Rabi flopping: role of the carrier-envelope phase. *Optics Letters*, *29*, 2160–2162.
- Naumov, S., Fernandez, A., Graf, R., Dombi, P., Krausz, F., & Apolonski, A. (2005). Approaching the microjoule frontier with femtosecond laser oscillators. *New Journal of Physics*, *5*, 216.
- Petek, H., & Ogawa, S. (1997). Femtosecond time-resolved two-photon photoemission studies of electron dynamics in metals. *Progress in Surface Science*, *56*, 239–310.
- Quail, J. C., Rako, J. G., Simon, H. J., & Deck, R. T. (1983). Optical second-harmonic generation with long-range surface plasmons. *Physical Review Letters*, *50*, 1987–1990.
- Raether, H. (1988). *Surface plasmons on smooth and rough surfaces and on gratings*. Berlin: Springer-Verlag.
- Reider, G. (2004). XUV attosecond pulses: Generation and measurement. *Journal of Physics D*, *37*, R37–R48.
- Ropers, C., Solli, D. R., Schulz, C. P., Lienau, C., & Elsaesser, T. (2007). Localized multiphoton emission of femtosecond electron pulses from metal nanotips. *Physical Review Letters*, *98*, 043907.
- Schoenlein, R. W., Fujimoto, J. G., Eesley, G. L., & Capeheer, T. W. (1988). Femtosecond studies of image-potential dynamics in metals. *Physical Review Letters*, *61*, 2596–2599.
- Simon, H. J., Mitchell, D. E., & Watson, J. G. (1974). Optical second-harmonic generation with surface plasmons in silver films. *Physical Review Letters*, *33*, 1531–1534.
- Siwick, B. J., Dwyer, J. R., Jordan, R. E., & Miller, R. J. D. (2003). An atomic-level view of melting using femtosecond electron diffraction. *Science*, *302*, 1382–1385.
- Stockman, M., Kling, M. F., Krausz, F., & Kleineberg, U. (2007). Attosecond nanoplasmonic field microscope. *Nature Photonics*, *1*, 539–544.
- Tóth, C., Farkas, G., & Vodopyanov, K. L. (1991). Laser-induced electron emission from an Au surface irradiated by single picosecond pulses at $\lambda = 2.94 \mu\text{m}$. The intermediate region between multiphoton and tunneling effects. *Applied Physics B*, *53*, 221–225.
- Tsang, T., Srinivasan-Rao, T., & Fischer, J. (1990). Surface-plasmon-enhanced multiphoton photoelectric emission from thin silver films. *Optics Letters*, *15*, 866–868.
- Tsang, T., Srinivasan-Rao, T., & Fischer, J. (1991). Surface-plasmon field-enhanced multiphoton photoelectric emission from metal films. *Physical Review B*, *43*, 8870–8878.
- Varró, S., & Farkas, G. (2008). Attosecond electron pulses from interference of above-threshold de Broglie waves. *Laser and Particle Beams*, *26*, 9–20.
- Yakovlev, V. S., Dombi, P., Tempea, G., Lemell, C., Burgdörfer, J., Udem, et al. (2003). Phase-stabilized 4-fs pulses at the full oscillator repetition rate for a photoemission experiment. *Applied Physics B*, *76*, 329–332.
- Yudin, G. L., & Ivanov, M. Y. (2001). Nonadiabatic tunnel ionization: Looking inside a laser cycle. *Physical Review A*, *64*, 013409.
- Zawadzka, J., Jaroszynski, D., Carey, J. J., & Wynne, K. (2000). Evanescent-wave acceleration of femtosecond electron bunches. *Nuclear Instruments & Methods in Physics Research, Section A*, *445*, 324–328.
- Zawadzka, J., Jaroszynski, D., Carey, J. J., & Wynne, K. (2001). Evanescent-wave acceleration of ultrashort electron pulses. *Applied Physics Letters*, *79*, 2130–2132.